Engineering of Robust Conjugated Polymer-Based Aerogels Via Surface-Initiated Polycondensation towards Sunlight-Driven Seawater Desalination and Uranium Extraction

Yuan Chen†, Guang-en Fu†, Yu-xiang Zhao, Ke Wang, Meng-wei Chen, Qiang Ma, Shan Li Jun-Yi Han Li-sha Liang, Wen-kai Zhao, Peng Xiao, Sheng Wang, Tao Chen*, Tao Zhang**

Y. Chen, G. Fu, Y. Zhao, K. Wang, M. Chen, Q Ma, S. Li, J. Han, L. Liang, W. Zhao, P. Xiao, Prof. Dr. T Chen, T. Zhang

Key Laboratory of Advanced Marine Materials, Ningbo Institute of Materials Technology and Engineering, Chinese Academy of Sciences, Ningbo 315201, China

E-mail: tao.chen@nimte.ac.cn; tzhang@nimte.ac.cn

Y. Chen, Prof. Dr. S Wang

School of Materials Science and Engineering, Zhejiang Sci-Tech University, Hangzhou 310018, China

E-mail: wangsheng@zstu.edu.cn

†Y. Chen, G. Fu contributed equally to this work

Supplementary Materials

Materials: Silica aerogel is purchased from Yanjin Chemical Building Materials Co., Ltd. 2,5-dihydroxyterephthalaldehyde (DHA) (95%), 4,4'-Biphenyldicarboxaldehyde,3,3'-dihydroxy (DBD) (97%), trifluoroacetic acid (99% AR), 1,4-Dioxane (99% AR), Acetonitrile (＞99% AR), (3-aminopropyl) triethoxysilane (APTES) (99%), $NaHCO_3$ (99.8% AR) and NaCl (99.5%

AR) were purchased from Aladdin Biochemical Technology Co., Ltd. 2,4,6-trimethyl-1,3,5-triazine (TMT) (98%) was purchased from Zesheng Technology Co., Ltd. 1,3,5-tris(4-formylphenyl) triazine (TFPT) (97%) was purchased from Alpha Chemical Co. Ltd. Mesitylene (97% AR) was purchased from Sahn Chemical Technology (Shanghai) Co., Ltd. Uranium nitrate (99%) and Arsenazo III (>95% AR) were purchased from Macklin Biochemical Co., Ltd. Unless otherwise stated, the commercially available reagents and solvents were used without further purification.

Supplementary Methods

Self-assembled monolayer (SAM) with amino groups

Silica aerogel substrate with a nanoscale oxide layer was washed extensively with ethanol and deionized water for 5 min and dried by a jet of dry argon, then was treated by oxygen plasma (PEC-6, 600 W, sykejing company) for 10 min. Afterward, the substrates were placed in a closed container with a vial containing 30 μL of 3aminopropyltrimethoxysilane. After the container was allowed to keep 80 °C for 2 h, the substrate was removed, washed with deionized water and ethanol then dried with a dry nitrogen stream.[1]

Synthesis of DHA-TMT sp^2C-CPP aerogel

2,4,6-trimethyl-1,3,5-triazine (TMT, 36.96 mg, 0.3 mmol) and 2,5-dihydroxyterephthalaldehyde (DHA, 74.76 mg, 0.45 mmol) and a mixture of mesitylene / 1,4-dioxane (1:1, v/v, 8 mL) were charged in a 100mL hydrothermal synthesis reactor. After addition of 2.5 mL trifluoroacetic acid, 0.3 mL acetonitrile and aminated silica aerogel substrates, the reaction mixture was ultrasonic treated to obtain a homogeneous suspension. The

reaction tube was then heated to 150°C under N_2 atmosphere for 3 days. After that, removed the reacting silica aerogel from the solution, washed with tetrahydrofuran and acetone. After cleaning, the silica aerogel is removed from the solution and dried under normal temperature to obtain the sp^2c-CPP aerogel.[2]

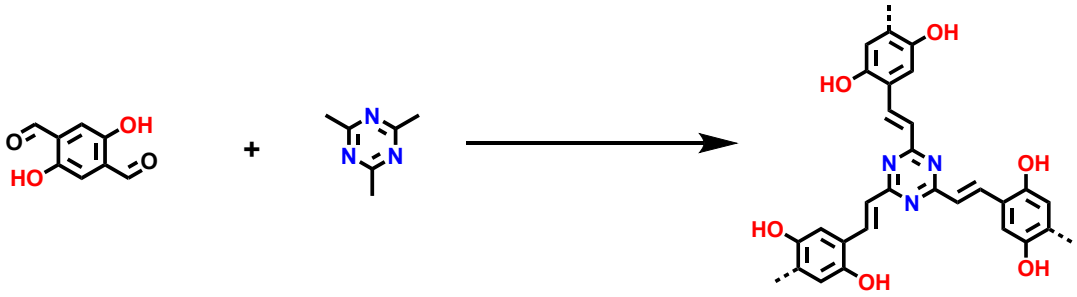

Scheme S1. Synthetic route towards DHA-TMT sp^2C-CPP.

Synthesis of DBD-TMT sp^2C-CPP aerogel

2,4,6-trimethyl-1,3,5-triazine (TMT, 36.96 mg, 0.3 mmol) and 4,4'-Biphenyldicarboxaldehyde,3,3'-dihydroxy (DBD, 109 mg, 0.45 mmol) and a mixture of mesitylene / 1,4-dioxane (1:1, v/v, 8 mL) were charged in a 100mL hydrothermal synthesis reactor. The following procedure is similar to the synthesis of DHA-TMT sp^2c-CPP on silica aerogel substrates.

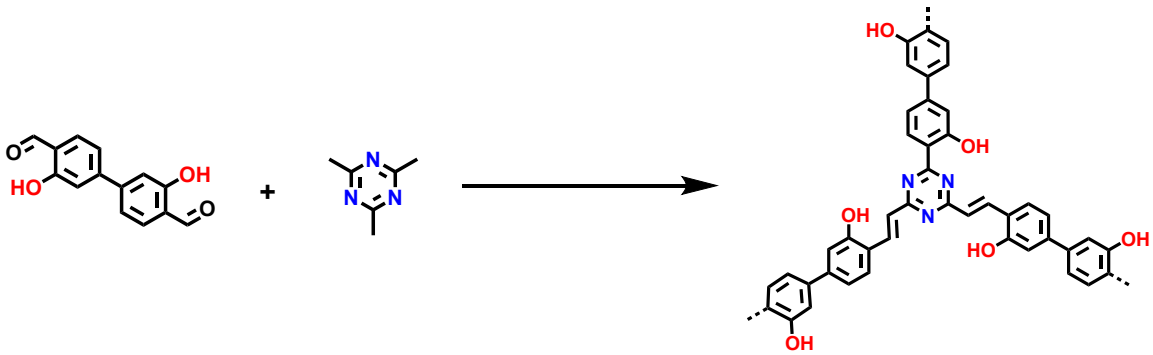

Scheme S2. Synthetic route towards DBD-TMT sp^2C-CPP.

Experimental processes and characterizations

Characterization: Infrared spectra (IR) were recorded on a Thermo NICOLET 6700

Intelligent Fourier infrared spectrometer. The scanning electron microscope (SEM) images were acquired using Cold field high resolution scanning electron microscope. Temperature versus time curves of DHA-TMT aerogels and DBD-TM aerogels and Infrared images were recorded using an optris PI400. The hydrophilic property of the sp^2C-CPP aerogel was observed on a contact angle measuring instrument (JY-82B Kruss DSA). UV-vis diffuse reflectance spectra (DRS) were recorded with a PE Lambda 900 UV/vis spectrophotometer at room temperature. X-ray photoelectron spectroscopy (XPS) was performed by using AXIS SUPRA spectrometer. The compression testing of sp^2C-CPP aerogel was conducted using platens on a universal testing machine (UTM 6103, SUNS, China) with a load cell of 1000 N and a stress rate of 2 mm min^{-1}.

Photothermal performance test

The evaporation rate of water and the efficiency of solar energy conversion in the photothermal evaporation process were measured comprehensively using the solar interface photothermal evaporation system.

Water evaporation performance experiments were conducted at a temperature of ~26 ℃ and a humidity of 40% using a xenon lamp (PL-X300DF, PLSS) with an AM 1.5G optical filter. The solar intensity was measured using a solar power meter (TES 132-SOLAR). The mass of the water loss is measured by an electronic balance (METTLER TOLEDO JJ324BF) with 0.1 mg resolution. Record the final mass change of feed water after 1 hour, and calculate the evaporation rate of water (ṁ) according to equation (1)

$$\dot{m} = \frac{m}{S} \tag{1}$$

Where m refers to the mass change recorded by the balance after 1 hour of illumination, S refers

to the surface area of the aerogel. During the solar evaporation process, each sample was infiltrated. According to formula (2), the solar photothermal conversion efficiency (η) in the process of photothermal evaporation was calculated

$$\eta = \frac{\dot{m} h_{LV}}{q C_{opt}} \quad (2)$$

Where ṁ refers to the water evaporation rate after subtracting evaporation rate under the dark circumstance, h_{LV} refers to the total liquid vapor phase-change enthalpy, q is the nominal solar intensity (1 kW m^{-2}), and C_{opt} represents the optical concentration.

After each desalination cycle, the CPP aerogel was immersed in DI water for 12 h and the water was changed every 2 h then used for next cycle.

Uranium extraction experiments

Arsenazo III determination of uranyl

Arsenazo III method was employed to determine uranyl concentrations in U-spiked deionized water unless otherwise indicated. Uranyl solution was added to Arsenazo III mixing solution containing deionized water (3 mL), Arsenazo III (0.2 mL, 1 mM) and HCl (0.8 mL, 0.1 M). After that, the absorbances at 652 nm were monitored by UV-vis spectrophotometer.

Photocatalytic reduction of U(VI) in laboratory

To evaluate the photocatalytic reduction effect on the uranium adsorption capacity, A 300W Xe lamp with a light density of 1 kW/m^2 was utilized as the simulated sunlight. A dark field environment was used for the control experiment.

Uranium extraction performance test

The photocatalysis system mainly consists of a sp^2c-CPP silica aerogel,200 mL beaker and a Xenon lamp. Spiked uranium solutions were prepared by dissolving uranyl nitrate hexahydrate

into simulated seawater (25.6 g L^{-1} NaCl, 193 mg L^{-1} $NaHCO_3$ PH=8.2). It was filtered using a 0.22 μm filter to remove particles and microorganisms. The solutio n held under magnetic stirring for different times with the stirring speed of 300 r/min. At each time point, an aliquot was taken out and analyzed using Arsenazo III Assay. The uranium adsorbing capacity was calculated using the following equation:

$$q_t = \frac{(C0 - C)\,V}{S} \tag{3}$$

where q_t is the amounts of adsorbed uranium at the exposure time (t); C_0 and C_t are the concentrations of uranium at time 0 and t, respectively; V is the volume of the solution (L) and S is the original area of the working material (m^2). At the equilibrium state, q_t and C_t are replaced by q_e and C_e, respectively

Adsorption kinetic models and parameters

The pseudo-second-order and pseudo-first-order models were analyzed by the following equations

$$\frac{t}{q_t} = \frac{1}{k_2 q_e^2} + \frac{t}{q_e} \tag{4}$$

$$\ln\left(q_e - q_t\right) = \ln q_e - k_1 t \tag{5}$$

where k_2 (g (mg min)$^{-1}$) and k_1 (min^{-1}) represent the corresponding rate constants.

Uranium adsorption behavior was also evaluated via adsorption isotherm experiment with different initial concentrations of uranyl (2, 4, 8, 16, 32 ppm). The equilibrium isotherm data were fitted by Langmuir (Equation (5)) and Freundlich (Equation (6)) models, respectively

$$\frac{C_e}{q_e} = \frac{C_e}{q_m} + \frac{1}{k_3 q_m} \quad (6)$$

where Ce is the equilibrium concentration (mg L-1), q_m is the saturated adsorption capacity (mg m^{-2}), and k_3 is an equilibrium constant related to the binding strength (L mg^{-1}).

$$\log q_e = \log k_4 + \frac{1}{n} \log C_e \quad (7)$$

where the constant k_4 is an approximate indicator of adsorption capacity, and 1/n is a function of the strength of adsorption in the adsorption process.

Supplementary Figures

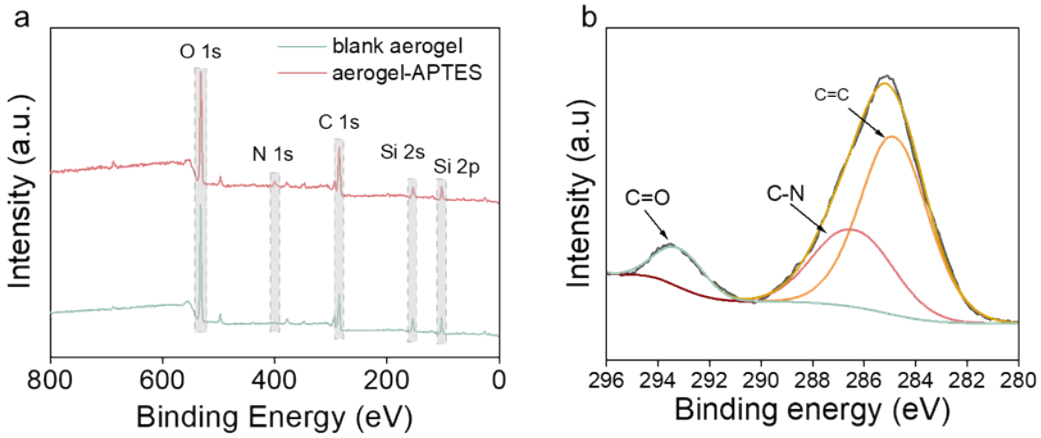

Fig. S1 (a) comprehensive XPS spectra, (b) high-resolution C 1s spectra of aerogel-APTES

The comprehensive XPS spectra and high-resolution C 1s spectra of aerogel-APTES reveal distinct new N 1s and C-N peaks, respectively, providing compelling evidence for the successful grafting of APTES onto the aerogels.

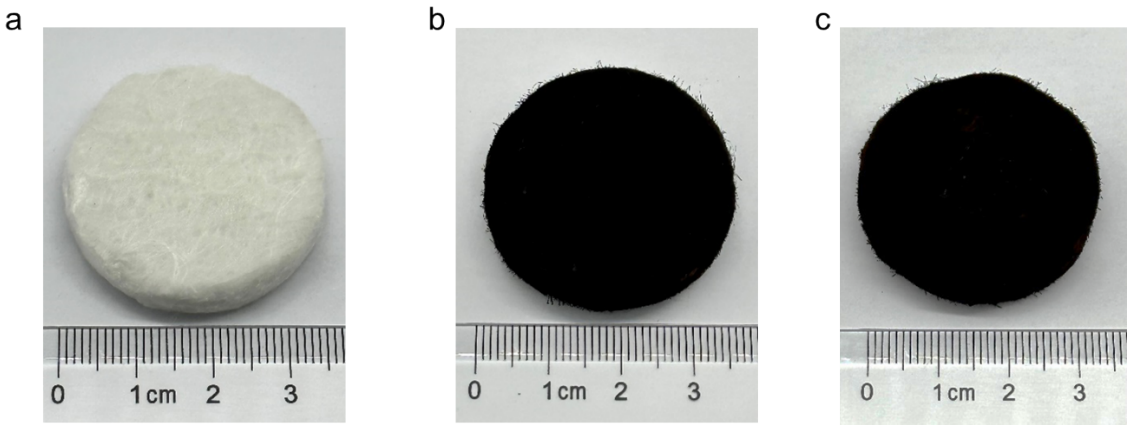

Fig. S2 Photograph of (a) silica aerogel, (b) DHA-TMT aerogel and (c) DBD-TMT aerogel.

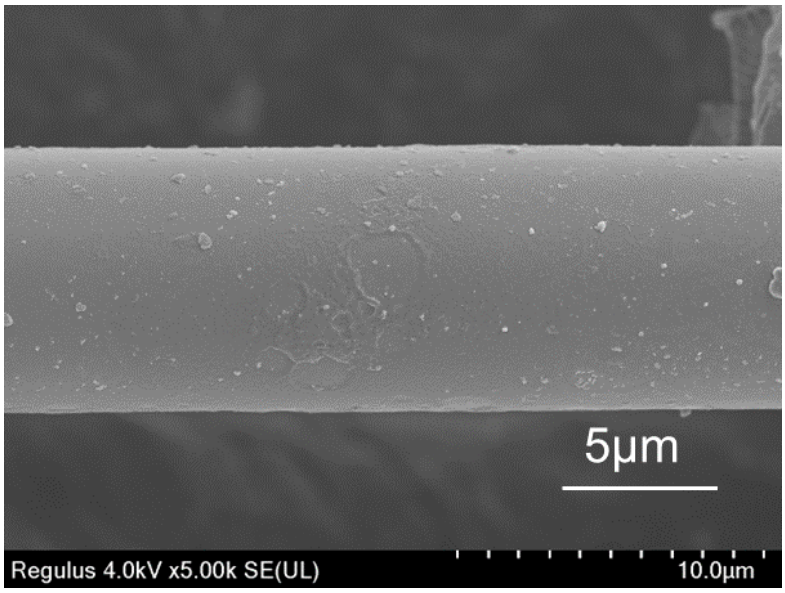

Fig. S3 Photograph and SEM images of blank silica aerogels.

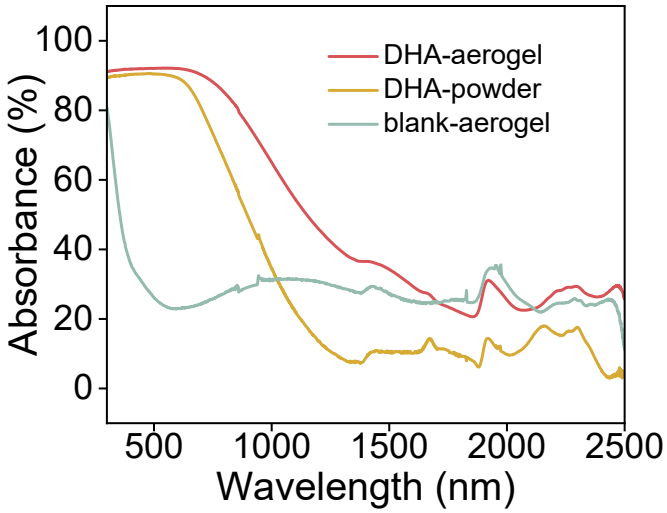

Fig. S4 The light absorption spectra of different samples in the wavelength range of 400 to 2500 nm.

DHA-TMT powder exhibit similar light absorption characteristics with the aerogel evaporators, which reveals that sp^2C-CPP plays a major role in photothermal and photocatalytic. The stronger light absorption of aerogels is due to the reflection of light in the 3D structure.

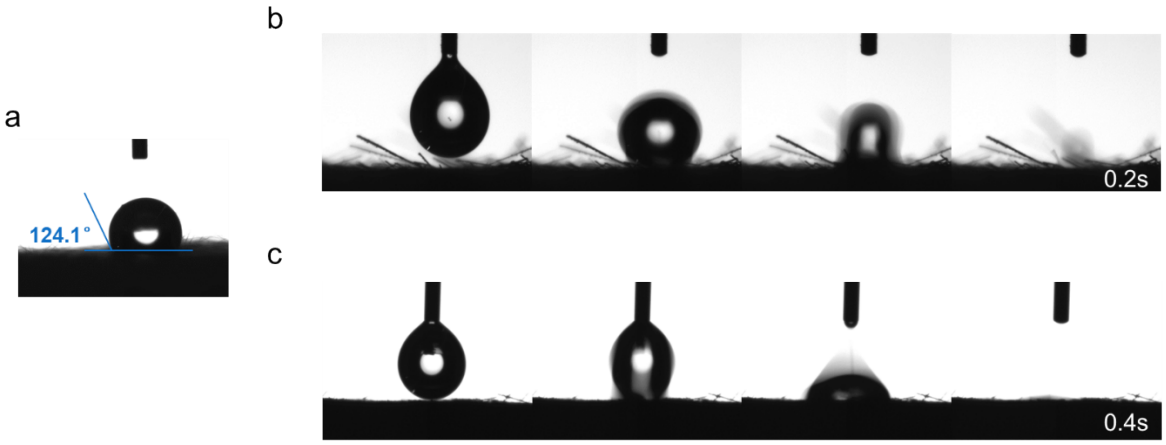

Fig. S5 The contact angles test for (a) silica aerogel, (b) DHA-TMT aerogel and (c) DBD-TMT aerogel.

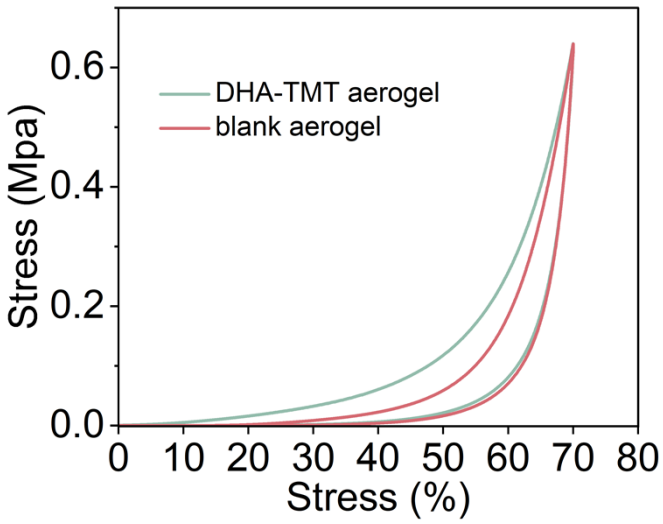

Fig. S6 The compression stress-strain curves of DHA-TMT aerogels and blank aerogel at strains of 70%.

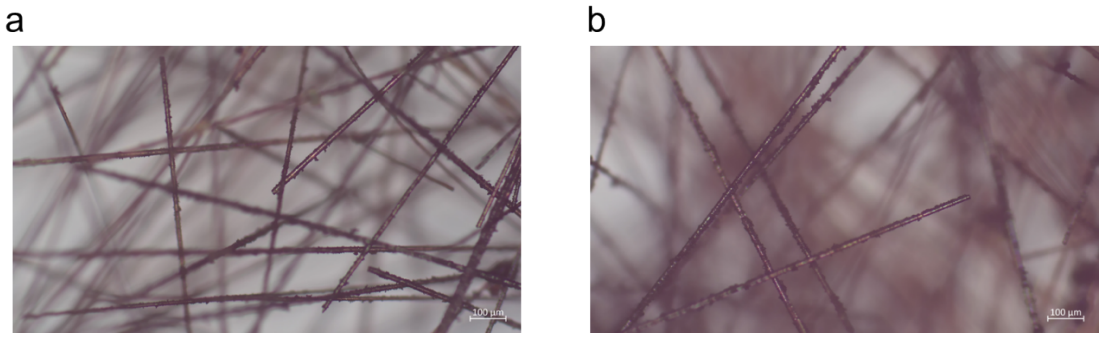

Fig. S7 The surface morphology of the sp^2C-CPP aerogel under optical microscope before (a) and after (b) compression fatigue testing.

The mechanical properties of the blank aerogel and DHA aerogel are similar, revealing that sp^2C-CPP coating has a relatively small impact on mechanical strength. Furthermore, the microscopic measurement demonstrated that sp^2C-CPP aerogel still retains fibrous structure after compression fatigue testing.

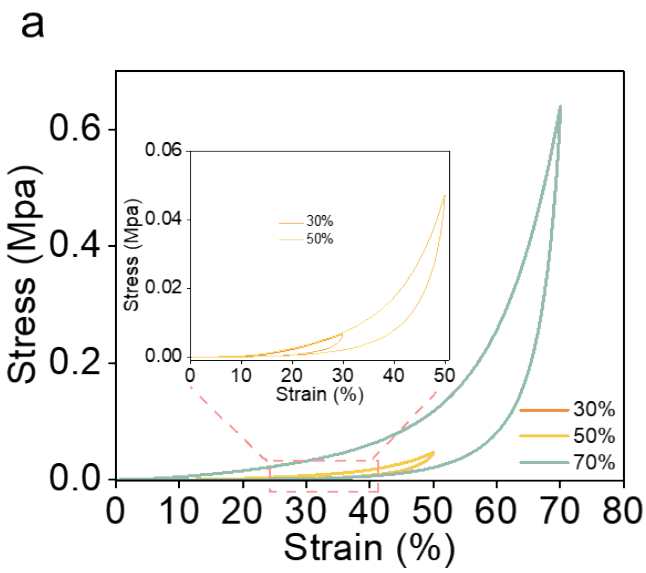

Fig. S8a The compression stress-strain curves of sp^2C-CPP aerogels at different strains of 30%, 50% and 70%.

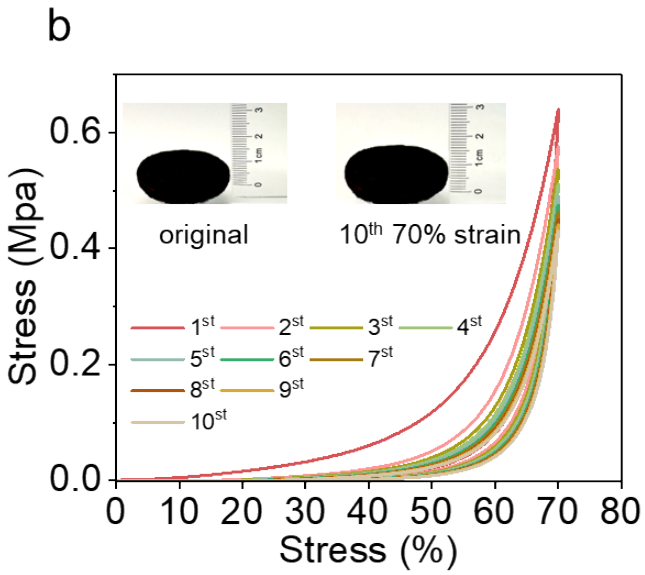

Fig. S8b Cyclic stress-strain curves of sp^2C-CPP aerogels at a strain of 70% with inset photographs showing the change of height after 10 test cycles.

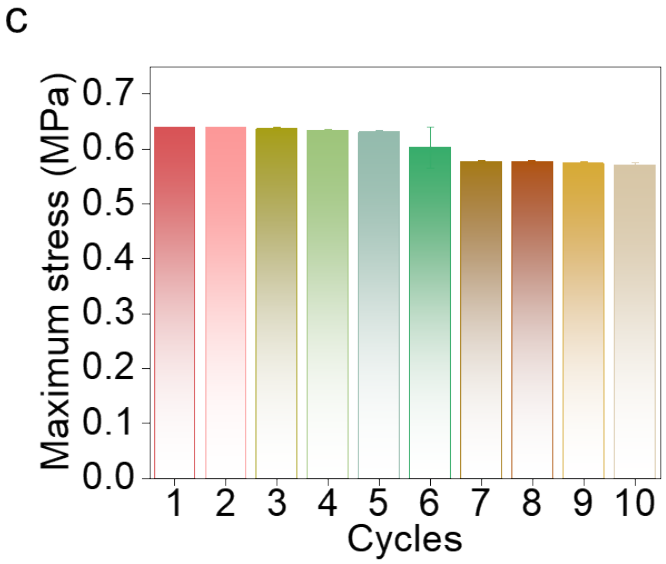

Fig. S8c The maximum stress of sp^2C-CPP aerogels in compression fatigue experiment at a strain of 70%.

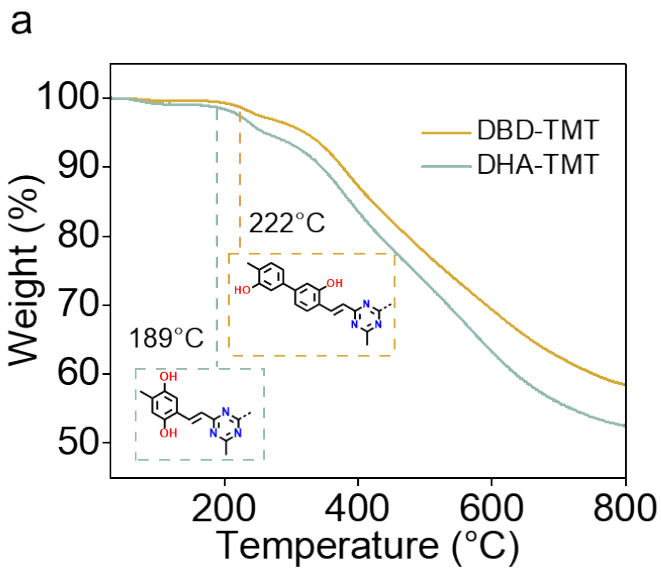

Fig. S9a Thermogravimetric analysis of DHA-TMT (green), DBD-TMT (yellow).

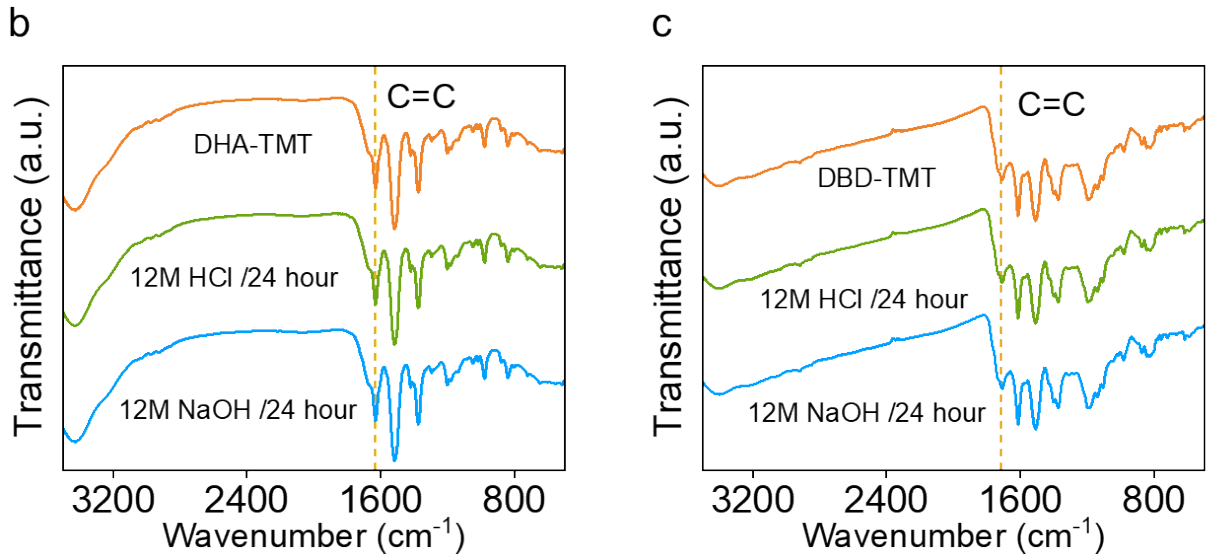

Fig. S9b-c Comparison of FT-IR spectra of DHA-TMT and DBD-TMT after treatment in 12 M HCl and 12 M NaOH for 24 hours.

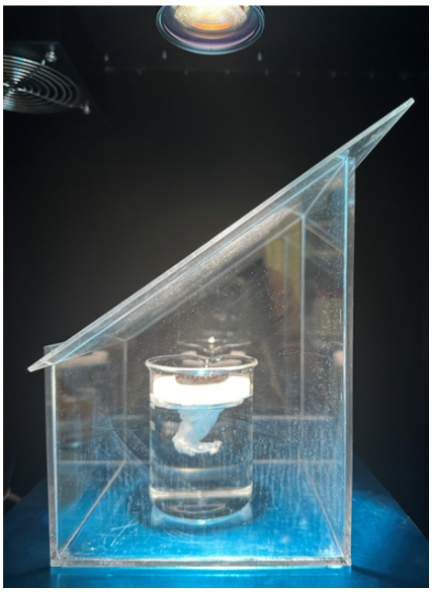

Fig.S10 Photograph of the setup for solar-driven clear water collection.

We put the evaporation device inside a homemade plastic container, as depicted in Figure S10 The inclined lid of this container allows for complete transmission of solar light. Subsequently, the generated water vapor condenses on the glass wall and eventually drips into the bottom of the glass container.

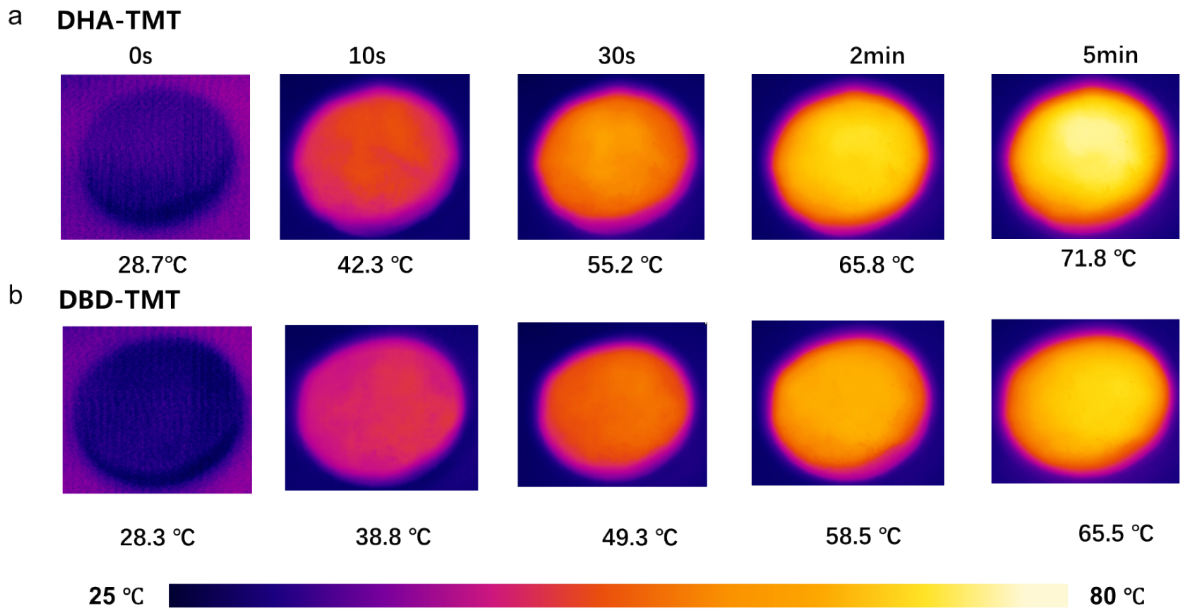

Fig.S11 IR images of (a) DHA-TMT aerogels and (b) DBD-TM aerogels under 1 sun irradiation for 5 minutes.

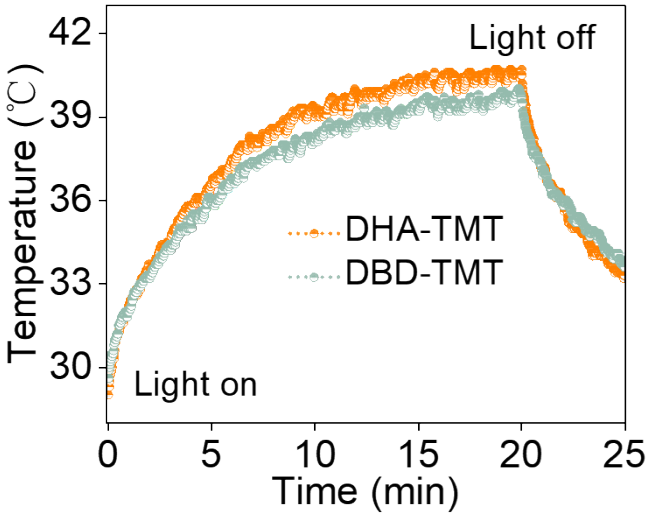

Fig.S12 Temperature versus time curves of DHA-TMT aerogels and DBD-TM aerogels filled with water.

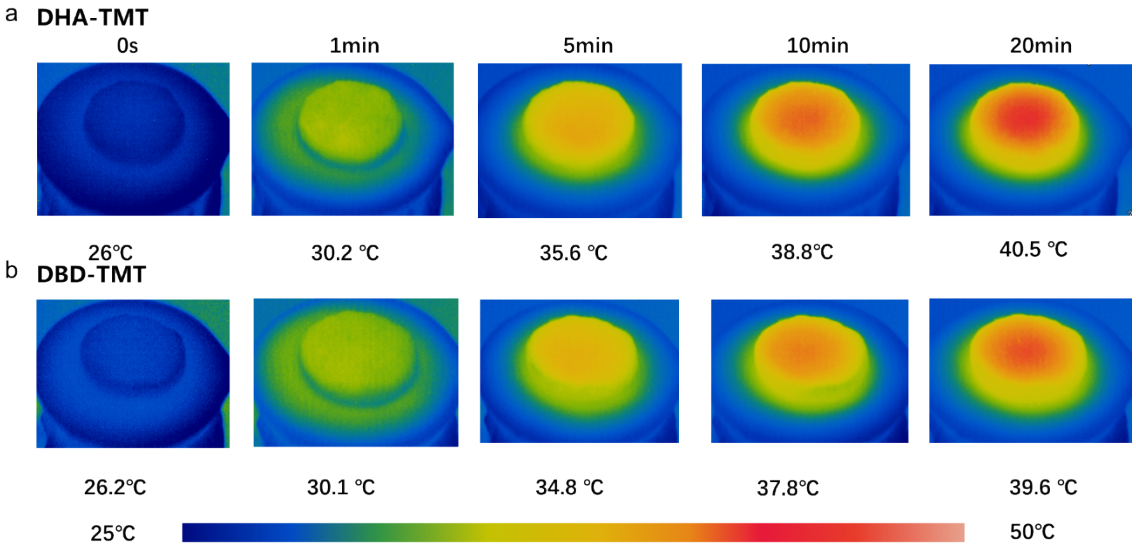

Fig.S13 IR images of (a) DHA-TMT aerogels and (b) DBD-TM aerogels filled with water under 1 sun irradiation for 20 minutes.

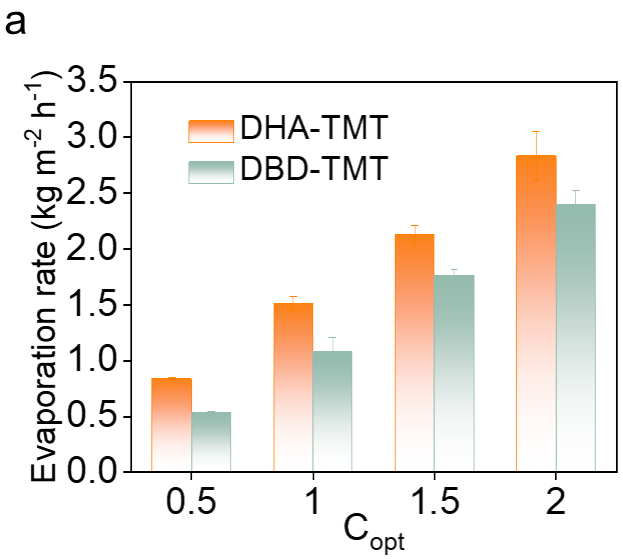

Fig.S14a Evaporation rate of the DHA-TMT aerogels and DBD-TMT aerogels under different optical concentrations

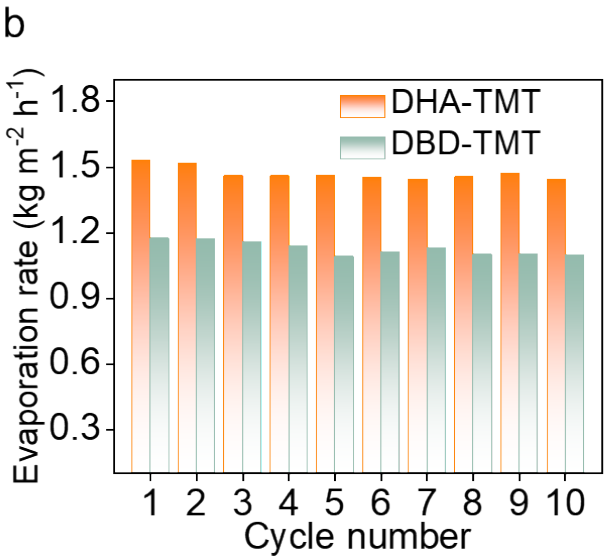

Fig.S14b Evaporation rate of the DHA-TMT aerogels and DBD-TMT aerogels under decacycle.

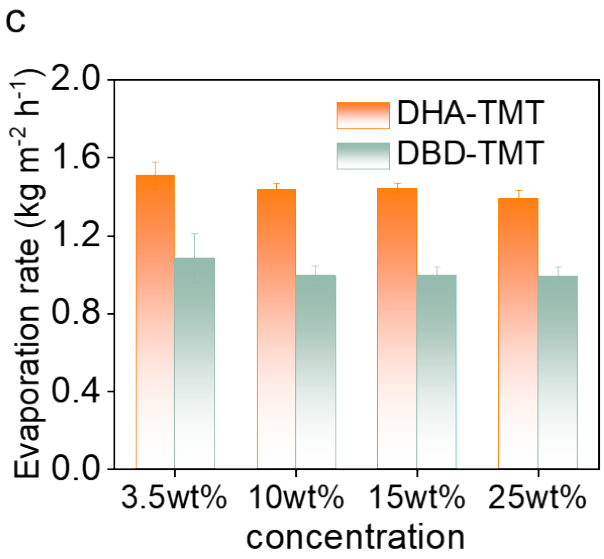

Fig.S14c Evaporation rate of the DHA-TMT aerogels and DBD-TMT aerogels under different simulated sea water concentrations.

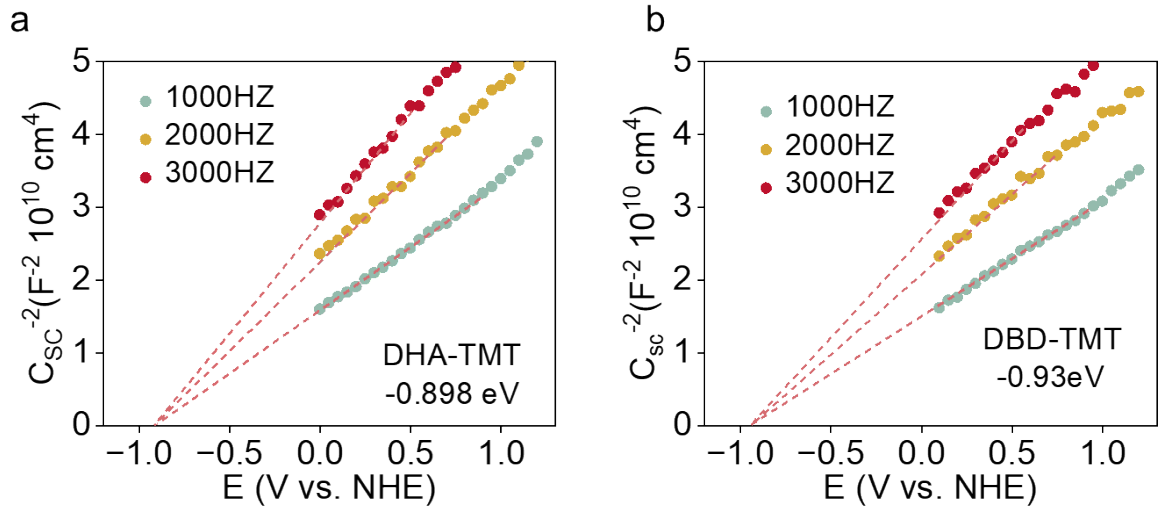

Fig.S15 Mott-Schottky plots of (a) DHA-TMT (b) DBD-TMT.

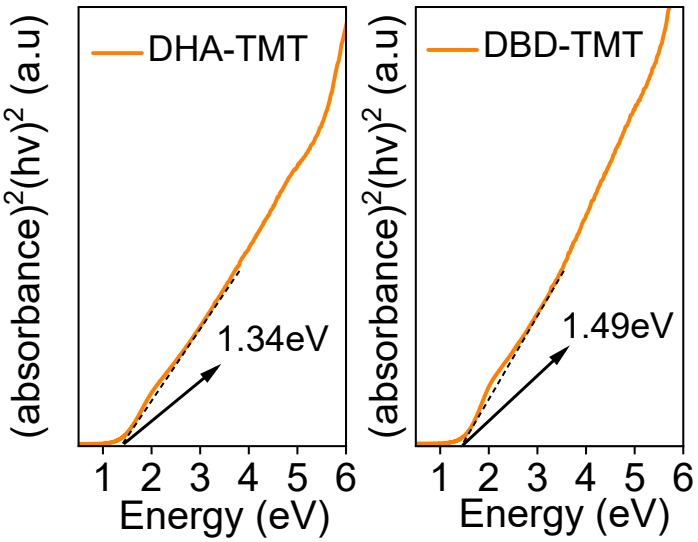

Fig.S16 Band gaps of DHA-TMT and DBD-TMT determined from the KubelkaMunk function.

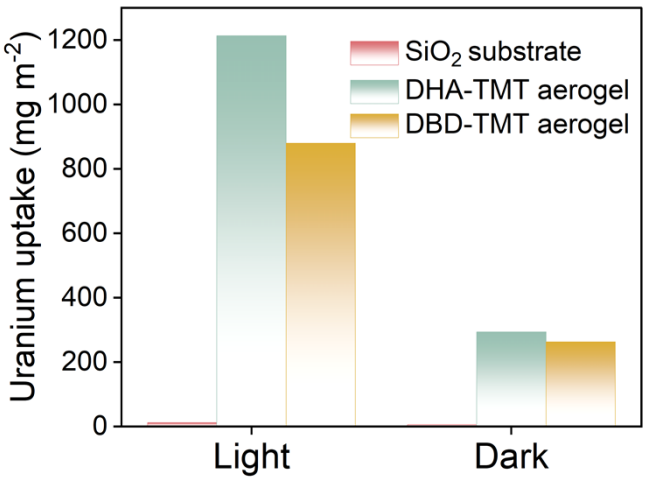

Fig. S17 The uranium extraction performance of SiO_2 aerogel substrate.

We tested the uranium capacity of SiO_2 aerogel substrate in the same condition. The results indicate that uranium capture by SiO_2 substrate almost negligible

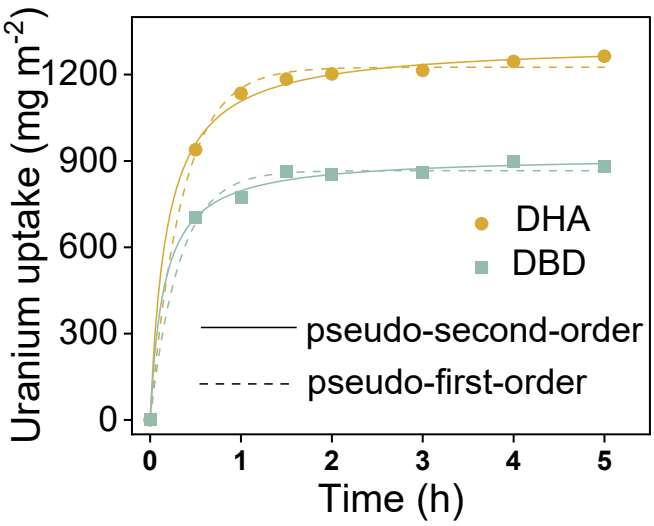

Fig. S18 Adsorption kinetic and the corresponding fitting curves based on pseudo-first-order and pseudo-second-order kinetic model for DHA-TMT (yellow) and DBD-TMT (green) in simulated seawater with 16ppm under simulated sunlight irradiation.

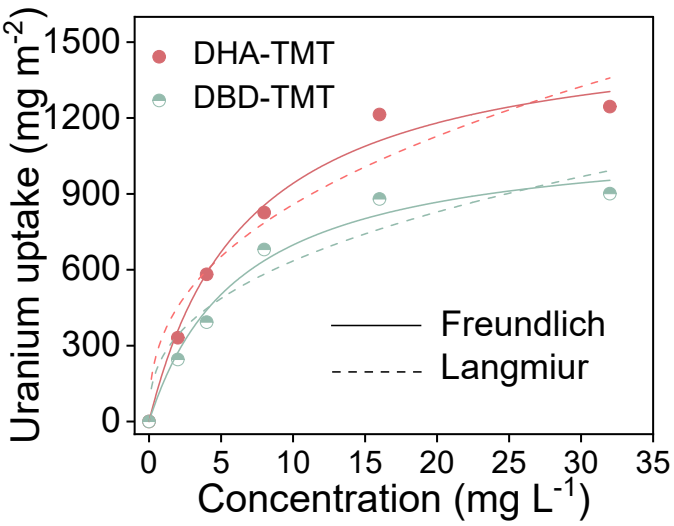

Fig. S19 Equilibrium adsorption isotherms of DHA-TMT (red) and DBD-TMT (green) adsorbent and the corresponding fitting curves based on Langmuir model and Freundlich model under simulated sunlight irradiation.

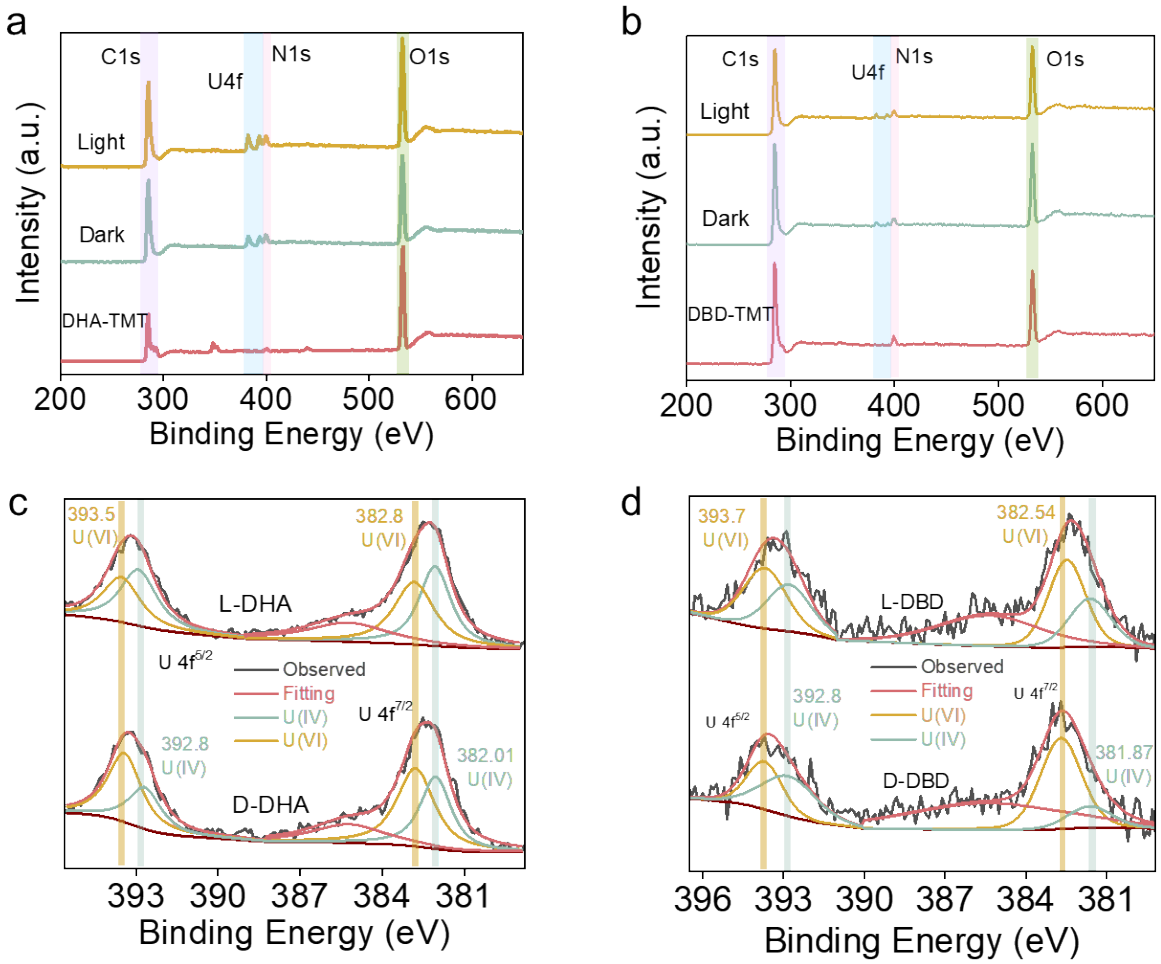

Fig. S20 (a-b) XPS survey spectra of DHA-TMT (left), DBD-TMT (right) measured before and after loaded with uranium under dark conditions and DHA-TMT (left), DBD-TMT (right) measured after loaded with uranium in the dark or under visible light irradiation. **(c-d)** U 4f high-resolution spectra of DHA-TMT-U (left), DBD-TMT-U (right) loaded with uranium in the dark or under visible light irradiation.

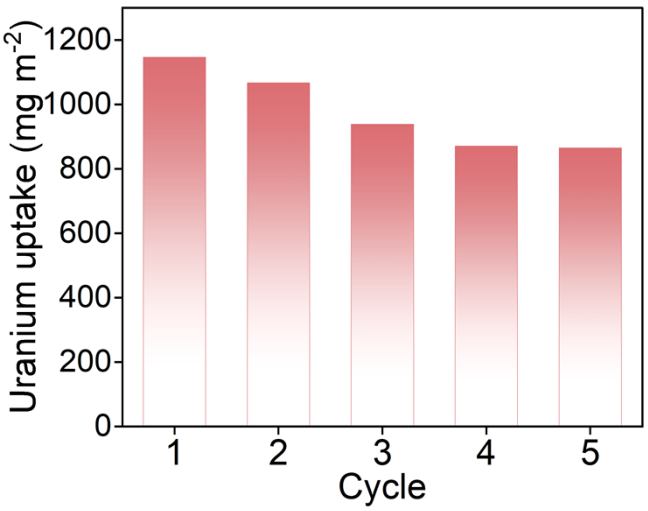

Fig. S21 Equilibrium adsorption capacity in five successive adsorption-desorption cycles.

Table 1 Comparison of evaporation performance and photothermal conversion efficiency of different evaporators based on two-dimensional materials previously reported.

Materials	**Evaporation ability ($Kg\ m^{-2}\ h^{-1}$)**	**photothermal conversion efficiency**	**Reference**
DHA-TMT	**~1.55**	**~95.6%**	**This work**
TPAD-COF	~1.42	~94%	[3]
GS-COF-1-3d	~1.38	~95.3%	[4]
GS-COF-2-7d	~1.34	~92%	[4]
PMDA-TAPA COF	~1.47	~97%	[5]
BHMS	~1.39	~84.7%	[6]
CPP	~1.5	~91.4%	[7]
GT-COF-3	~1.314	~90.7%	[8]
VA-MXA	~1.46	~87%	[9]
GS-POP-2	~1.42	~96.8%	[10]
BG@MS12	~1.42	~89.4%	[11]

Reference

[1] X. Yin, D. Wu, H. Yang, J. Wang, R. Huang, T. Zheng, Q. Sun, T. Chen, L. Wang, T. Zhang, *ACS Macro Lett.* **2022**, *11*, 693.

[2] W.-R. Cui, C.-R. Zhang, R.-H. Xu, X.-R. Chen, W. Jiang, Y.-J. Li, R.-P. Liang, L. Zhang, J.-D. Qiu, *Appl. Catal. B Environ.* **2021**, *294*, 120250.

[3] X. Yan, S. Lyu, X. Xu, W. Chen, P. Shang, Z. Yang, G. Zhang, W. Chen, Y. Wang, L. Chen, *Angew. Chem. Int. Ed.* **2022**, *61*, e202201900.

[4] Z. Chen, Y. Su, X. Tang, X. Zhang, C. Duan, F. Huang, Y. Li, *Sol. RRL* **2021**, *5*, 2100762.

[5] X. Li, Y. Pang, Y. Zhang, B. Ge, J. Liu, Y. Zhang, L. Zhao, G. Ren, Z. Zhang, *Sep. Purif. Technol.* **2023**, *326*, 124804.

[6] W.-R. Cui, C.-R. Zhang, R.-P. Liang, J. Liu, J.-D. Qiu, *ACS Appl. Mater. Interfaces* **2021**, *13*, 31561.

[7] W.-R. Cui, C.-R. Zhang, R.-P. Liang, J.-D. Qiu, *J. Mater. Chem. A* **2021**, *9*, 25611.

[8] X. Tang, Z. Chen, Q. Xu, Y. Su, H. Xu, S. Horike, H. Zhang, Y. Li, C. Gu, *CCS Chem.* **2022**, *4*, 2842.

[9] Q. Zhang, G. Yi, Z. Fu, H. Yu, S. Chen, X. Quan, *ACS Nano* **2019**, *13*, 13196.

[10] Y. Su, Z. Chen, X. Tang, H. Xu, Y. Zhang, C. Gu, *Angew. Chem. Int. Ed.* **2021**, *60*, 24424.

[11] M. Wang, Y. Wei, X. Wang, R. Li, S. Zhang, K. Wang, R. Wang, H. Chang, C. Wang, N. Ren, S.-H. Ho, *Nat. Water* **2023**, *1*, 716.